



**HAL**  
open science

## Atomic scale microstructural insights of superconducting $\beta$ -tungsten thin films

Ananya Chattaraj, Manju Mishra Patidar, V. Ganesan, Sébastien Joulie,  
Virginie Serin, Alain Claverie, Vijay Kumar, Alope Kanjilal

► **To cite this version:**

Ananya Chattaraj, Manju Mishra Patidar, V. Ganesan, Sébastien Joulie, Virginie Serin, et al.. Atomic scale microstructural insights of superconducting  $\beta$ -tungsten thin films. *Journal of Materials Research*, 2022, 10.1557/s43578-022-00803-y . hal-03853337

**HAL Id: hal-03853337**

**<https://hal.science/hal-03853337>**

Submitted on 15 Nov 2022

**HAL** is a multi-disciplinary open access archive for the deposit and dissemination of scientific research documents, whether they are published or not. The documents may come from teaching and research institutions in France or abroad, or from public or private research centers.

L'archive ouverte pluridisciplinaire **HAL**, est destinée au dépôt et à la diffusion de documents scientifiques de niveau recherche, publiés ou non, émanant des établissements d'enseignement et de recherche français ou étrangers, des laboratoires publics ou privés.

# Atomic Scale Microstructural Insight of Superconductivity in $\beta$ -Tungsten Thin Films

Ananya Chattaraj<sup>1</sup>, Manju Mishra Patidar<sup>2,3</sup>, V. Ganesan<sup>2,4</sup>, Sébastien Joulie<sup>5</sup>, Virginie Serin<sup>5</sup>,

Alain Claverie<sup>5</sup>, Vijay Kumar<sup>6,7</sup>, and Alope Kanjilal<sup>1\*</sup>

<sup>1</sup>*Department of Physics, School of Natural Sciences, Shiv Nadar University, NH-91, Tehsil Dadri,*

*Gautam Buddha Nagar, Uttar Pradesh 201 314, India*

<sup>2</sup>*UGC-DAE Consortium for Scientific Research, Khandwa Road, Indore, Madhya Pradesh 452001,*

*India*

<sup>3</sup>*Emerald Heights International School, A.B. Road, Indore, Madhya Pradesh 453331, India*

<sup>4</sup>*Medi-Caps University, Indore A.B. Road, Pigdamber, Rau, Indore, Madhya Pradesh 453331, India*

<sup>5</sup>*CEMES-CNRS and Université de Toulouse, 29 rue J. Marvig, 31055 Toulouse, France*

<sup>6</sup>*Center for Informatics, School of Natural Sciences, Shiv Nadar University, NH-91, Tehsil Dadri,*

*Gautam Buddha Nagar, Uttar Pradesh 201 314, India*

<sup>7</sup>*Dr. Vijay Kumar Foundation, 1969 Sector 4, Gurgaon, Haryana 122 001, India*

## ABSTRACT

The importance of atomic structure in illustrating the exotic superconductivity, especially the critical transition temperature ( $T_c$ ) and upper critical magnetic field  $H_{c2}(0)$  of electron beam deposited  $\beta$ -tungsten ( $\beta$ -W) thin films is reported. There is a significant change in  $T_c$  and  $H_{c2}(0)$  with the variation of the film thickness.  $T_c$  and  $H_{c2}(0)$  for a low thickness ( $\sim 35$  nm) film are measured to be  $\sim 3.14$  K and 10.72 T, whereas for a comparatively thicker ( $\sim 60$  nm) film, the values are 1.38 K and 2.34 T, respectively. The evolution of the  $\beta$  phase of W has been identified by grazing incidence X-ray diffraction and from that, the crystallite size, and strain

have also been calculated. The atomic arrangement and microstructure of the deposited  $\beta$ -W films have been probed using transmission electron microscopy which shows the formation of self-assembled columns in both the films. The corresponding high-resolution images manifest an improvement in crystallinity of the nanoscale grains in a disordered matrix with increasing film thickness. Moreover, a drastic change in the atomic structure corresponding to two different thickness films is found to be associated with the change in the oxygen concentration as revealed from energy-dispersive X-ray spectroscopy. This is further supported by *ab initio* calculations. Based on the intricate atomic structure and microstructure, the underlying superconductivity has been discussed in light of the existing models.

**Keywords:**  $\beta$ -phase tungsten, thin films, microstructure, disorder, superconductivity

**\*Corresponding author:** [aloke.kanjilal@snu.edu.in](mailto:aloke.kanjilal@snu.edu.in)

## INTRODUCTION

The  $\alpha$  phase of tungsten (W) with body-centered cubic (BCC) structure is a well-known type-I elemental superconductor with a critical superconducting transition temperature ( $T_c$ ) of 0.01 K.<sup>1</sup> But its allotrope  $\beta$ -W with A15 structure has received overwhelming interest because of its exotic superconducting behavior that includes a higher  $T_c$  of  $\sim 3$ -4 K and its sustainability at higher upper critical magnetic fields ( $H_{c2}$ ).<sup>2,3,4,5,6</sup> There is a long-standing interest in materials with the A15 structure such as Nb<sub>3</sub>Ge for high magnetic field dependent applications and especially for their usage in superconducting magnets.<sup>7,8</sup> Given the A15 structure,  $\beta$ -W is also promising, although its structural stability is considered to be dictated by the presence of impurities such as oxygen.<sup>9,10,11,12,13</sup>

Earlier, superconductivity has been observed in  $\beta$ -W films by tunneling method and the structure has been analyzed by X-ray diffraction (XRD).<sup>6</sup> In another study an enhancement in the value of  $T_c$  was reported in W-based amorphous thin films by incorporating 5 to 70 at.% metalloids, with a parallel verification of their thermal stability.<sup>3</sup> Attempts have also been made to understand the effects of structural instability on superconductivity due to the exposure of A15 superconducting compounds to high-energy laser.<sup>14</sup> Kammerer and Strongin<sup>15</sup> have also studied superconductivity in W films prepared by (i) electron beam (at a pressure of  $2 \times 10^{-6}$  Torr) and (ii) sputter (in argon atmosphere) deposition techniques. They found a maximum  $T_c$  of  $\sim 4.1$  K in a film of about 200 nm thickness and also measured the critical magnetic field. The structure of these films was examined by both XRD and electron microscopy. From these measurements they separated out the effects of strain and particle size. However, no conclusion was established on the observed line broadening. Two possible reasons were proposed for the higher  $T_c$  in these films: (i) the presence of surface oxygen and the existence of oxide metal interface, and (ii) the presence of disorder,<sup>15</sup> although these were not so clearly manifested to understand the underlying superconductivity. In another study, an enhancement of

superconductivity related parameters in W films was also found and it was discussed in the light of structural changes<sup>16</sup> Superconductivity has also been reported<sup>2</sup> in low dimensional structures, such as electron beam grown W nanowires, though it is vulnerable to ion beam-produced defects. Majkova *et al.*<sup>17</sup> further studied the superconducting properties of amorphous W/Si multilayers, where they demonstrated an almost linear rise in  $T_c$  with the increasing number of layers. There are some other studies based on the superconducting fluctuations in amorphous WSi.<sup>18,19</sup> As superconductivity in low dimensional systems is believed to be somewhat ruled by the growth conditions, a clear understanding of the microstructure including the local atomic structure is very essential not only for a fundamental understanding but also for future applications, especially for oxygen-induced  $\beta$ -W. Although, the discovery of  $\beta$ -W was made a long time ago,<sup>5,20,21</sup> an understanding of the formation and stability of this phase has been quite challenging. It has been found that oxygen plays a crucial role in stabilizing  $\beta$ -W.<sup>4,11,12</sup> The role of oxygen in this phase formation has been recently discussed in detail by a combined experimental and theoretical study<sup>22</sup>. The solution energy of O in  $\beta$  is significantly higher compared to  $\alpha$  and this leads to the stabilization of the  $\beta$  phase with oxygen doping.<sup>22</sup> The presence of oxygen leads to disorder in the local atomic structure and this is further enhanced with an increasing number of dopants (>20 at.%).<sup>22,23</sup> Therefore, it is difficult to recognize and explain the observed superconductivity in  $\beta$ -W truly without having a detailed understanding of the elemental distribution and their influence on the atomic structure.

In the present study, we have measured the exotic superconductivity of  $\beta$ -W thin films and analysed it in the light of the microstructure of the films for the purpose of not only applications but also to achieve a fundamental understanding. Several films were grown by electron beam deposition technique with varying film thickness. Among them, two best quality films have been used for further low-temperature measurements, where it has been found that

$T_c$  and  $H_{c2}(0)$  vary with film thickness. Also, based on the atomic structure we found a  $T_c$  (1.38 K) which does not belong to either  $\alpha$ -W or  $\beta$ -W, and has not been found earlier. This value of  $T_c$  is very useful for developing photon number resolving transition-edge sensors for astronomical and quantum information applications as well as for usage in a cryogenic particle detectors.<sup>24,25</sup> The phase formation and corresponding structures of the deposited films with two different thicknesses have been studied in detail through grazing incidence XRD (GIXRD) and transmission electron microscopy (TEM) investigations. The structures become disordered due to the presence of O which is revealed from the energy dispersive X-ray spectroscopy (EDX),<sup>22,23</sup> and further confirmed from *ab initio* calculations. Using these results and observations, the effect of the atomic structure in the underlying superconductivity of  $\beta$ -W is well recognized.

## EXPERIMENTAL METHODS

A 500  $\mu\text{m}$  thick Si (100) wafer was diced into pieces of area  $1 \times 1 \text{ cm}^2$  and cleaned by dipping in trichloroethylene, acetone, isopropanol, and deionized water followed by heating for 2 min in each step. After chemical cleaning of the Si substrate, W films were grown at room temperature (RT) by electron beam deposition technique with a deposition rate of 0.01 nm/s. The chamber base pressure was  $\sim 5 \times 10^{-7}$  Torr and it was maintained at  $\sim 1 \times 10^{-6}$  Torr during deposition. Around 99.95% pure W powder (Alfa Aesar) was used to deposit W thin films. The thickness of the deposited films was estimated by a surface profilometer (DektakXT, Bruker). The evolution of the  $\beta$ -W phase was confirmed by GIXRD using Cu- $K_\alpha$  radiation ( $\lambda = 0.154$  nm) from a D8-Discover (Bruker) instrument. The detailed microstructural investigation was carried out by TEM in both plan-view and cross-sectional geometries using a  $C_s$  corrected Tecnai-FEI system operated with an acceleration voltage of 200 kV. The electrical transport measurements down to 2K and 14T magnetic fields were carried out by conventional four probe measurements with a dc current of 100  $\mu\text{A}$  using 14T/2K PPMS system from Quantum

Design USA. For measurements below 2K, a dilution refrigerator insert from the same Quantum Design was used. This was equipped with an ac resistance measurement configuration. A drive frequency of 12.2 Hz with the same current level in four probe configuration was employed. Typical current densities used are 280 A/cm<sup>2</sup> for a low thickness (~35 nm) film and 114 A/cm<sup>2</sup> for higher thickness (~60 nm) film.

## CALCULATION DETAILS

The atomic structure of  $\beta$ -W with and without oxygen was studied from *ab initio* calculations. We performed simulated annealing with *ab initio* molecular dynamics on bulk  $\beta$ -W having different concentrations of oxygen. The atomic structures were fully optimized. The details of the *ab-initio* calculations have been given in Ref. [22]. The electronic densities of states, which are influenced by the atomic structure have been also calculated and analyzed with and without the doping of oxygen in  $\beta$ -W.<sup>23</sup>

## RESULTS

### *Atomic Structure*

We considered two film thicknesses of ~35 nm (W35) and ~60 nm (W60) in this study. The GIXRD patterns of W35 and W60 films in the range of  $2\theta$  from 10° to 80° are shown in Fig. 1. As discerned, the broad peak centered at ~40° in W35 creates an ambiguity in A15  $\beta$ -W phase identification (JCPDS file #00-047-1319) as it signifies the presence of a disordered structure. Such a broad reflection is associated with the formation of a disordered  $\beta$ -W phase when the oxygen concentration is increased above 25 at.%.<sup>22</sup> However, the characteristic reflections from the (200), (210), and (211) planes of  $\beta$ -W (A15 structure) are identified in W60 film having lower (~16 at.%) oxygen concentration<sup>22</sup> compared with the W35 film. It should be noted here that the  $\alpha$ -W(110) reflection (JCPDS#04-0806) is expected to overlap

with the  $\beta(210)$  peak due to their close proximity. Another weak and broad peak with its maximum at  $\sim 70^\circ$  is found in W35 film, but three different reflections can be distinguished in W60 film, namely  $\beta(222)$ ,  $\beta(320)$ , and  $\beta(321)$  (JCPDS file #00-047-1319). It can be seen in Fig. 1 that the peak corresponding to  $\beta(210)$  for W35 film shifts to slightly lower  $2\theta$  value compared to the one in W60. This is in agreement with the results from simulated oxygen doped W bulk which show an increase in the lattice parameter with an increase in oxygen concentration. The sharp peak at  $\sim 52^\circ$  (indicated by \*) is the reflection from the Si substrate.<sup>26</sup>

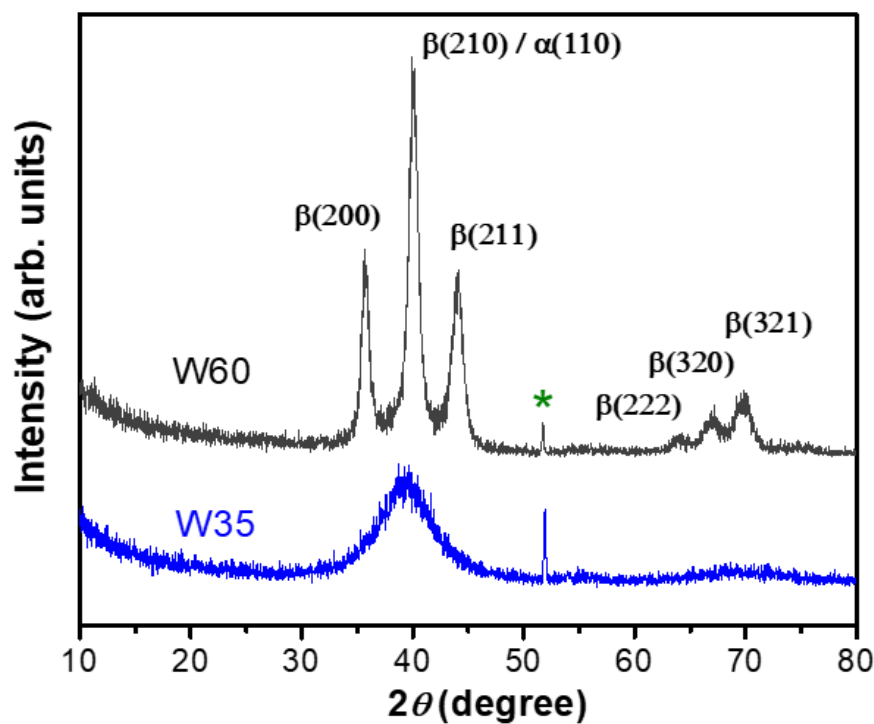


**Figure 1.** Typical GIXRD patterns of W35 and W60 films. Different peaks in the case of W60 have been identified with the  $\beta$ -W phase. The peak indicated by \* represents the reflection from the Si substrate.

The strain and average crystallite size in the film have been calculated from the GIXRD data by using Williamson-Hall (W-H) equation,

$$b \cos \theta = 0.9\lambda/D + 4\varepsilon \sin \theta, \quad (1)$$

where  $b$  is the full-width at half maximum (FWHM) of a diffraction peak,  $\varepsilon$  is the strain,<sup>27,28</sup> and  $D$  is the average crystallite size. The W-H equation basically gives a straight line, from where we can extract the average crystallite size and strain from the intercept and slope, respectively. The diffraction peaks for both W35 and W60 are fitted in a standard software and their FWHMs are extracted. Using six distinct diffraction peaks in W60, the W-H equation is employed for determining  $\varepsilon$  and  $D$  (see Fig. S1 in Supporting Information). Because of the availability of only a couple of broad peaks (absence of sufficient numbers of reflections), the W-H equation is not suitable for W35 film. Instead, we have used the Scherer equation for determining the average crystallite size,

$$D = 0.9\lambda/(b\cos\theta) \quad (2)$$

and the associated strain  $\varepsilon = b/(4 \tan\theta)$ .<sup>29</sup> The results are summarized in Table 1. In this case, the instrumental broadening is corrected by using the formula  $b = [(b_M)^2 - (b_I)^2]^{0.5}$  where  $b_M$  and  $b_I$  are the FWHMs of the measured and standard peaks, respectively. Here, the strain is found to be increased with decreasing crystallite size. Therefore, the observed broadening in the XRD peaks is due to the size effect of the crystallites, especially the absence of long-range order with small (~1.5 nm) crystallites in W35 film.

*Table 1. Average crystallite size ( $D$ ) and strain ( $\varepsilon$ ) determined from the recorded GIXRD patterns of W35 and W60 films.*

Films	W35	W60
$D$ (nm)	1.47	22.84
$\varepsilon$	0.070	0.006

To achieve a comprehensive knowledge of the structural evolution with increasing W film thickness, further investigations have been made by TEM. A typical bright-field cross-sectional

TEM (XTEM) image of W35 is displayed in Fig. 2(a), showing the formation of self-assembled columnar structure. A close inspection indicates the appearance of a very thin natural oxide ( $\text{SiO}_x$ ) layer at the W/Si interface, while high-resolution (HR) XTEM image in Fig. 2(b) further confirms its thickness of  $\sim 3$  nm. One can further distinguish the formation of a disordered W film, and this continues up to the surface [see Fig. 2(c)]. However, it shows some dark patches (highlighted by yellow dashed curves) along with short-range atomic ordering in the adjacent regions (marked by downward arrows). This is again reflected in the plan-view TEM (PVTEM) image [see Fig. 2(d)]. Here, few  $\beta(200)$  planes are evidenced, where a typical inter-planar spacing is marked by yellow lines. As  $\beta$ -W phase is found to be stable in the presence of oxygen, the films were further diagnosed by EDX in cross-sectional mode. The measurements have been done in both ways; along the surface (in different depths) and perpendicular to the surface.<sup>22,23</sup> In any case, a nearly uniform distribution of O throughout the film was manifested, and a typical EDX image in Fig. 2(e) shows the superimposition of the signals from W, O, and Si elements across the film. One can see from Fig. 2(e) that Si did not diffuse in the W film, but oxygen is found to be distributed all over. The average atomic concentration of oxygen across the film is found to be reduced from  $\sim 20$  at.% to  $\sim 16$  at.% by increasing film thickness from 35 nm to 60 nm.

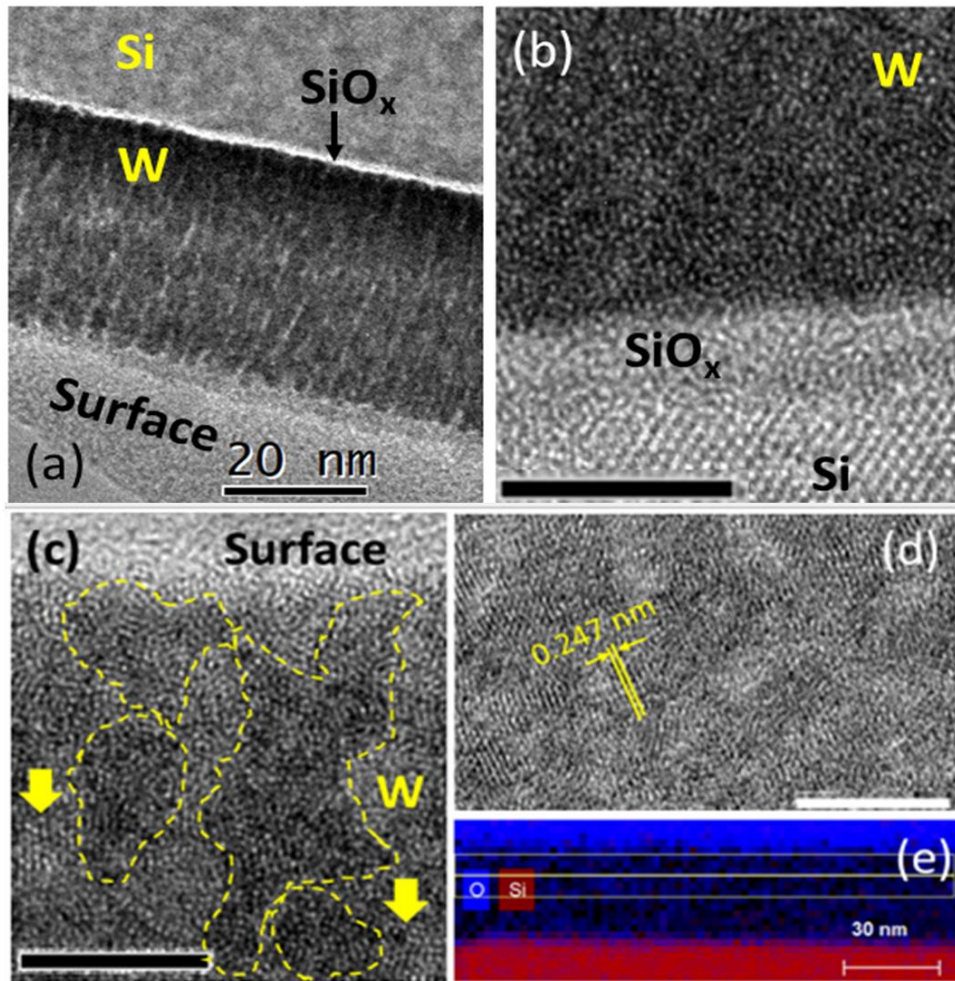


**Figure 2** (a) The bright-field XTEM image of W35 in low magnification, showing the formation of columnar structures (dark gray) in W film, while the natural oxide ( $\text{SiO}_x$ ) layer of Si below the W film is shown by an arrow. (b) HR-XTEM image of the W/Si interface, revealing the disordered structure in the W film on an amorphous ( $\sim 3$  nm thick)  $\text{SiO}_x$  layer. (c) Another HR-XTEM image of the near surface region of W film, displaying randomly shaped dark patches (some of them highlighted by yellow dashed curves) along with short range local ordering in the adjacent regions (marked by downward arrows). (d) The granular columns with atomic ordering at their boundaries are also visible in HR-PVTEM image, where the inter-planar spacing of the  $\beta(200)$  planes is indicated by parallel yellow lines. The scale bars in (b), (c), and (d) are of 5 nm. (e) The EDX imaging analysis in the cross-sectional mode displays superimposed distributions of the W (black), O (blue) and Si (red) elements across the film.

Figure 3 shows a comparison of the microstructure features in W35 and W60 films. In comparison with W35, a distinct change in microstructure is noticed in W60. Owing to similar magnification, one can easily compare the difference in the average grain size from the PVTEM and XTEM images in Figs. 3(a) and (b), respectively. In fact, the HRTEM images display well separated columns in W35, but most of them are found to be connected with the neighboring ones in W60 due to relative increase in average grain size [see Fig. 3(a)]. A close inspection of Fig. 3(b), however, reveals that the grains are more prominent and extended up to the Si substrate in W60 while the columns in W35 film are granular in nature. Intriguing short range atomic ordering is also noticed in W35, as can be realized from the inset in Fig. 3(b). In contrary, big crystallites ( $> 20$  nm) are formed in W60 film, which is also in good agreement with our GIXRD result (Fig. 1 and Table 1). A drastic change in atomic ordering is also observed from the inset of the lower panel of Fig. 3(b). The increase in the average crystallite size in W60 film is further reflected from the selected area electron diffraction (SAED) patterns in Fig. 3(c). The bright spots in the polycrystalline rings of the recorded SAED pattern of W60 are the signature of the formation of relatively bigger crystallites. Moreover, the rings are fitting well with the  $\beta$ -W phase according to JCPDS file #03-065-6453.<sup>30</sup> On the other side, the SAED of W35 film exhibits a bright ring surrounded by several diffused rings. Here, the arrays of bright spots superimposed on these rings show the reflections from the Si substrate. Considering the bright ring and its adjacent diffused rings into account, the calculated interplanar spacing ( $d$ ) values of  $\sim 0.201$  nm, 0.229 nm, and 0.247 nm suggest reflections from the (211), (210), and (200) planes of the partially crystalline  $\beta$ -W grains. Since the  $d$  spacing values of  $\alpha(110)$  and  $\beta(210)$  are  $\sim 0.223$  nm and 0.225 nm, it is impossible to discard the existence of the former one.<sup>31</sup> The analysis of the remaining rings is, however, not straightforward because of their diffusive nature arising from poor atomic ordering in small grains. However, the approximate  $d$  spacings for the remaining rings has been estimated to be

$\sim 0.142$  nm,  $0.129$  nm, and  $0.114$  nm, which can be related to the reflections from the  $\beta(222)/(320)$ ,  $\beta(321)/(400)$ , and  $\beta(420)/(421)$  planes, respectively. Similarly, reflection from the  $\alpha(211)$  planes is also expected with  $\beta(321)/(400)$ . All the rings are indexed accordingly for clarity.

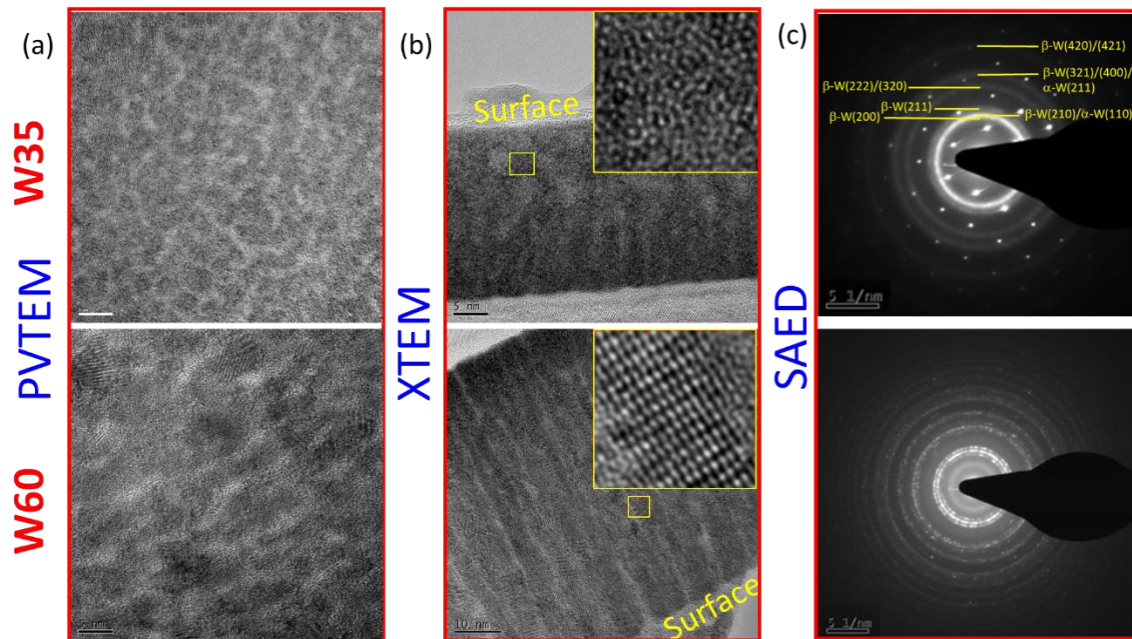


**Figure 3.** (a) High-resolution PVTEM and (b) XTEM images of W35 (top row) and W60 (bottom row) films. The magnified images of the regions (marked by yellow boxes) in the figure (b) are projected in the respective insets, showing the disordered and ordered structures in the respective grains of W35 and W60 films. The scale bar in (a) is 5 nm for both the films, while 5 nm and 10 nm for XTEM images of W35 and W60, respectively. The SAED patterns of the respective films are shown in (c), confirming the polycrystalline nature of  $\beta\text{-W}$  phase though prominent in W60. The different rings are also indexed for W35. The arrays of bright spots (upper panel) superimposed on these rings show the reflections from the Si substrate.

Figure 4(a) displays a perfectly aligned plane in  $\beta\text{-W}$  along the  $[001]$  zone axis with a square lattice structure in W60. The average distance between the bright spots is estimated to be  $\sim 5.1 (\pm 0.03)$  Å which is also well reproduced<sup>22,23</sup> by our *ab initio* calculations on pure  $\beta\text{-W}$ .

The first Fourier transformation (FFT) of the square lattice is also shown in the inset, where the spots are indexed according to the  $\beta$ -W phase. The changes in the contrast however suggests a complex structure when focus is changed [Fig. 4(b)]. A close inspection depicts the presence of distorted icosahedral structures, though it is prominent near the grain boundary. Interestingly, this feature looks like the ones observed in W35, although they are randomly arranged [see inset, Fig. 2(b)].

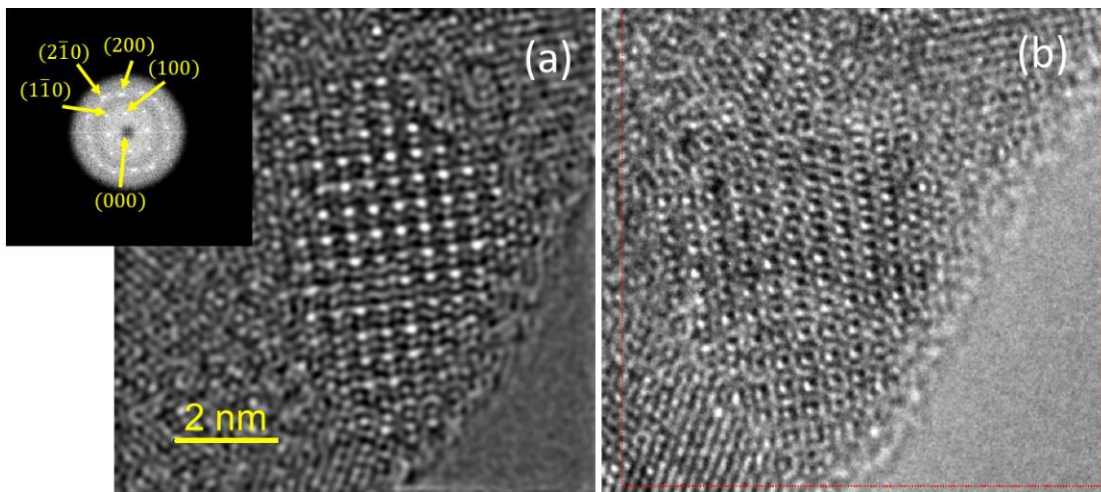


**Figure 4.** (a) A square lattice structure is found in W60 in HRTEM image, whereas (b) shows the same grain at different focus, showing the location of the additional atoms in the unit cells. The FFT of the square lattice in (a) is shown in the inset, where all the diffraction spots are perfectly indexed according to  $\beta$ -W phase.

The evolution of  $\beta$ -W phase was also examined by *ab initio* molecular dynamics calculations based on density functional theory. We studied doping of 10 to 40 at.% oxygen in the supercells of  $\alpha$ - and  $\beta$ -W. The lattice parameters as well as the ionic positions were fully relaxed after simulated annealing run. It was found that the favorable position of oxygen is the tetrahedral interstitial site (TIS) to sit in the A15 structure. The corresponding cohesive energy, lattice parameters, bond lengths, etc. have been optimized and discussed in detail in Ref. [22]. It is revealed that the lattice parameters are slightly stretched by increasing oxygen doping

concentration and this lead to a disordered structure. However, the structure remains intact for comparatively low O doping cases. From the calculations, we found that the degree of disorder depends not only on the O doping concentration, but also on the distribution of oxygen in the lattice. Clustering of oxygen was found to be favorable and therefore in a sample with less than ~15 at.% O concentration, there is likely to be a coexistence of  $\alpha$  and  $\beta$  phases. This can be also recognized from the GIXRD and TEM results of film W60.

### ***Low temperature resistivity***

To verify the superconducting behavior of the W films, low temperature electrical resistivity ( $\rho$ ) was measured with and without a magnetic field. The data in the absence of the external magnetic field for both W35 and W60 films are shown in Fig. 5. The superconducting transition temperatures are found to be ~3.10 K and ~1.40 K for W35 and W60 films, respectively. This thickness dependent transition in the resistivity is the major finding in the present study. In order to understand this intriguing phenomenon, we further explored the behavior of resistivity under a magnetic field.

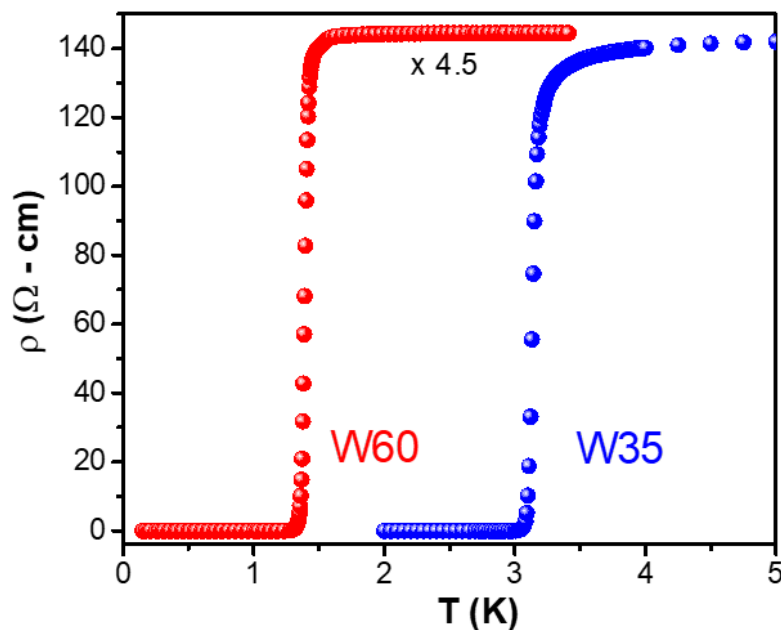


**Figure 5.** Temperature variation of resistivity for  $\beta$ -W films at zero magnetic field.

## Resistivity under magnetic field

The resistivity has also been measured with an applied magnetic field and the corresponding  $d\rho/dT$  has been also calculated for further analysis. These are shown in Figs. 6(a) and (b), respectively, for the W35 film while the same for the W60 film are presented in Figs. 7(a) and (b).

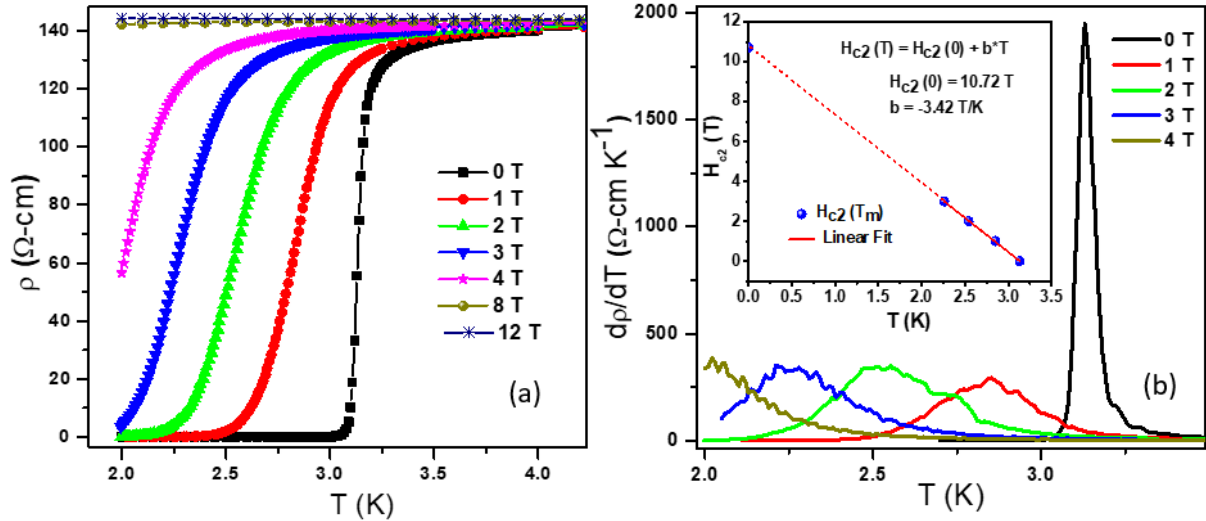


**Figure 6.** (a) Temperature variation of  $\rho$  of  $\beta$ -W35 film under an applied magnetic field up to 12 T shows broadening in resistivity with increasing field. Results for zero magnetic field case are also shown. (b) The temperature derivative of  $\rho$  as a function of temperature under different applied magnetic fields. Inset shows the plot of the critical field  $H_{c2}$  as a function of temperature. The red line indicates a linear fit.

In the case of W35, one can see from Fig. 6(a) that  $\rho$  starts to fall from 3.9 K ( $T_{PP}$ ) itself while it drastically drops below 3.33 K ( $T_{on}$ , the onset of superconductivity) and it completely vanishes below 2.92 K ( $T_{c0}$ ). The corresponding mid-point of the transition or mean field transition temperature ( $T_m$ ) is  $\sim 3.14$  K. We should note here that the  $T_m$  is also denoted by the peak in the  $d\rho/dT$  vs  $T$  plot [see Fig. 6(b)]. As the transition in the critical region is almost sharp, therefore here it is considered that  $T_m \sim T_c$ , superconducting critical transition

temperature. It is also clear from Fig. 6(a) that the  $T_c$  gradually shifts to lower values with increasing magnetic field. As discerned from Fig. 6(b), a sharp peak is visible at  $\sim 3.14$  K for zero magnetic field, while a gradual enhancement in transition width is found with increasing magnetic field. Moreover, the critical magnetic field with respect to temperature is also displayed in the inset and the observed linear behavior will be discussed in the following.

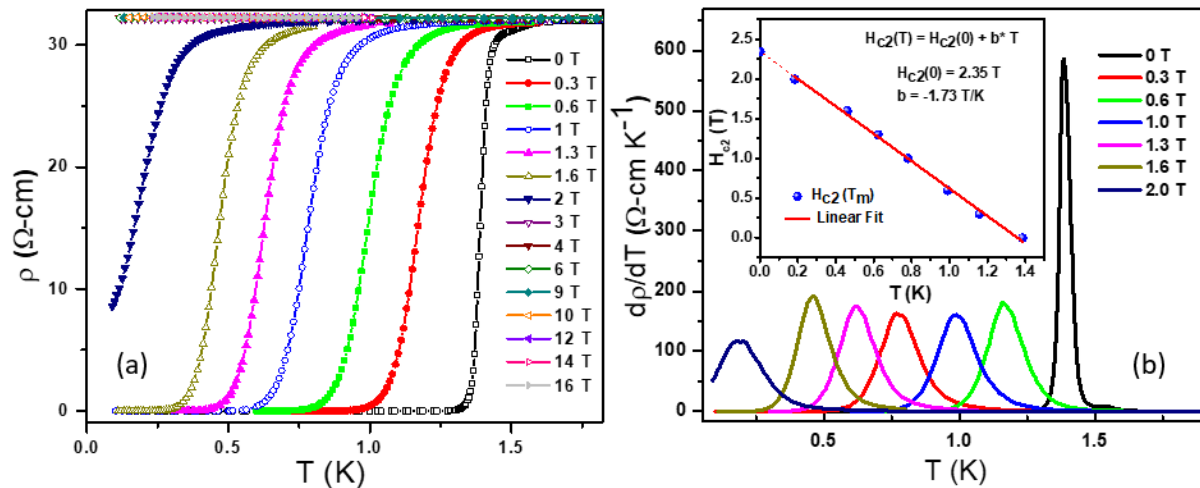


**Figure 7.** (a) Temperature variation of  $\rho$  for W60 film for applied magnetic fields up to 16 T. Data show broadening in  $\rho$  with increasing field. (b) The temperature derivative of  $\rho$  as a function of temperature under different magnetic fields up to 2 T. Inset shows the plot of the critical field as a function of temperature. The red line indicates a linear fit.

As in the case of the W35 film,  $T_c$  is found to shift towards lower values with increasing magnetic field in W60 film also [see Fig. 7(a)]. Moreover, a sharp peak is visible at  $\sim 1.38$  K in Fig. 7(b) for zero magnetic field. This is the  $T_c$  for the W60 film. The corresponding transition points as well as the temperatures related to various stages of transitions for the W35 and W60 films are listed in Table 2. The superconducting transition width taken from  $d\rho/dT$  is found to be almost the same (see Table 2), signifying a sharp transition as in conventional superconductors. However, more broadening is seen in W35 film as compared to W60 due to

the disordered structure. Likely in W35 film, the critical magnetic field is also found to be following a linear trend with temperature for the W60 film [inset, Fig. 7(b)].

Table 2: Various indicators of the transition temperatures for the W35 and W60 films.

Sample	$T_{PP}$ (K)	$T_{on}$ (K)	$T_m$ (K)	$T_{c0}$ (K)
W35	3.90	3.33	3.14	2.92
W60	2.09	1.53	1.38	1.18

### ***Critical magnetic field***

The  $H_{c2}(0)$  value determined from the variation of  $H_{c2}$  as a function of  $T$  [inset, Fig. 6(b)] for the W35 film is estimated to be  $\sim 10.72$  T by extrapolating the fitted data. Interestingly, the temperature variation of  $H_{c2}$  is found to be a linear function rather than the one expected from the conventional BCS theory,

$$H_{c2} = H_{c2}(0) \left[ 1 - \left( \frac{T}{T_c} \right)^t \right] \quad (3)$$

Using this equation, the fitting process gives the value of  $t$  as 1.07. Using the Werthamer-Helfand-Hohenberg (WHH) equation

$$H_{c2}(0) = -0.693 T_c \left( \frac{dH_{c2}}{dT} \right)_{T_c} \quad (4)$$

we find the value of  $H_{c2}(0)$  to be  $\sim 8.35$  T for the W35 film. The temperature variation of  $H_{c2}$  is also plotted in the inset of Fig. 7(b) for the W60 film, where  $H_{c2}(0)$  is determined to be  $\sim 2.34$  T by extrapolating the fitted data. In this case the WHH estimate yields the value of  $H_{c2}(0)$  to be  $\sim 1.64$  T.

### ***Coherence length***

The coherence length  $\xi$  of W35, a type-II superconductor, is estimated to be  $\sim 5.3$  nm from

$$\xi^2 = \frac{\phi_0}{2\pi H_{c2}(0)} \quad (6)$$

where the quanta of flux  $\phi_0 = \frac{hc}{e} \approx 2.067 \times 10^{-15}$  Wb.<sup>42</sup> Here, the calculated  $\xi$  is found to be higher than the average crystallite size of  $\sim 1.47$  nm in the W35 film as listed in Table 1. However, an estimate of the coherence length  $\xi$  for the W60 film turns out to be 11.83 nm, which is less compared to the projected average crystalline grain size of  $\sim 22.84$  nm.

## DISCUSSION

Our results show that the W35 film has a long-range disordered structure yet organized microstructure with a higher internal strain and  $T_{c0} \sim 2.92$  K. However, comparatively ordered  $\beta$  phase with lower strain provides a  $T_{c0} \sim 1.18$  K. These results point towards the involvement of microstructure and associated strain in controlling  $T_c$ , in accordance with the prior studies.<sup>32,33,34,35,36</sup> In fact, Pogrebnyakov *et al.*<sup>33</sup> reported an increase in  $T_c$  by introducing epitaxial tensile strain in MgB<sub>2</sub>. Precipitation induced appearance of internal strain was also proposed to justify the increase in  $T_c$ .<sup>34</sup> Chloe Herrera *et al.*<sup>36</sup> further discussed the strain engineered appearance of superconducting phases in SrTiO<sub>3</sub>. However, in most of the cases, an epitaxial layer was only considered to explain the role of strain on superconductivity. In the present case also, a higher  $T_c$  ( $\sim 3$  K) has been detected in the W35 film in the presence of a relatively higher strain (see Table 1) in granular structure. Since the strain can affect lattice vibrations and heat capacity,<sup>37,38</sup> it is expected to modulate phonon dispersion and hence the phonon density of states. As a matter of fact, it has a direct impact on  $T_c$  according to the standard Bardeen–Cooper–Schrieffer (BCS) theory.<sup>39,40</sup> However, the atomic structures in the present case, especially the atomic ordering and average grain size and shape are the decisive factors for controlling the superconducting phenomenon in the W35 and W60 films. The effect

of disorder on  $T_c$  has also been reported in a few theoretical studies.<sup>41,42</sup> One such study emphasized that the anisotropy in the order parameter of a superconductor plays an important role in its response to impurities, where both the inter-band and intra-band impurity scattering processes are considered.<sup>41</sup>

The grains are quite small in the case of the W35 film (see Table 1). They are especially smaller than the obtained coherence length (5.3 nm) and therefore the volume of a grain is lesser than the coherence volume. It characterizes the existence of a conventional superconductivity. However, the number of Cooper pairs is not so large like in a conventional BCS superconductor as the number of grains is small ( $\sim 2$ ) within a coherence length in this case. Under this circumstance, two consecutive grains are separated by an insulating medium, mostly due to the involvement of oxygen at the grain boundaries (see Fig. 3). This intermediate thin oxide medium ultimately participates in electron tunnelling from one grain to another and in turn takes part in changing the physical property of the entire system. Even, depending on this narrow tunnelling medium the electronic coupling would be either strong or weak and subsequently control  $T_c$ . It is somewhat similar to the Mott-type metal-insulator transition.<sup>43</sup> A similar explanation was proposed by Kammerer and Strongin in an earlier study.<sup>15</sup> However, due to the lack of the structural analysis, it was not established there.

Additionally, a long-range disorder also exists in the W35 film. It is well known that the disordered type superconductors follow the Anderson type transition.<sup>41,42,43</sup> However, in this case the disorder is not homogeneous as the presence of short-range crystallites cannot be ignored. Based on the microstructural analysis, we can instead infer that the granular superconductivity is dominated in the W35 film as compared to only disorder-based transition. This is quite similar to the case superconductivity in granular Al.<sup>44</sup> Whereas in the W60 film, the volume of the average crystalline grain is higher than the coherence volume, even of the order of  $2\xi$ . Therefore, this can be considered as an unconventional superconductor. In fact,

due to the short coherence length, tunnelling of electrons between the grains is difficult in this case, and in turn  $T_c$  gets reduced. The upper critical magnetic field has also been found to be anisotropic and is dependent on film thickness. This signifies the deviation from the standard 3D BCS formalism. It even also deviates from the predictions for the temperature dependence of  $H_{c2}$  calculated by WHH. This is due to the corrections needed in the standard BCS formalism to describe superconductivity in a two-dimensional superconductor, as shown by Tinkham, especially for thin films.<sup>45</sup> Tinkham<sup>45</sup> also discussed the importance of inhomogeneities in the superconducting films for achieving unusual behaviour in the presence of impurities by impeding the free movement of flux quanta. Considering these facts, we believe from the present experimental work that the structural modification and the associated strain, and the corresponding effect in microstructures with varying oxygen concentration as a function of film thickness led to the observed superconductivity.

## SUMMARY

In summary, our results show that the  $T_c$  is higher ( $\sim 3.14$  K) for the low thickness (W35) film, whereas it reduces to  $\sim 1.38$  K in the thicker (W60) film. In the former case there is a long-range disorder associated with a higher strain. The orderliness in the structure is basically controlled by the oxygen concentration as supported by our *ab initio* calculations. Though there is no significant change in the transition width, a slight increase in field induced resistive broadening in the W35 film is due to the presence of disorder. The analysis of the results led to two main understanding: (i) the impact of internal strain on the critical transition temperature  $T_c$  and superconductivity in  $\beta$ -W thin films in the absence of external magnetic field. In particular, the strain has been shown to be released by reducing the mean oxygen concentration from  $\sim 20$  to  $\sim 16$  at.% with increasing film thickness from 35 nm (W35) to 60 nm (W60) (ii) The average grain size and the grain boundaries along with the involved atomic structures are

found to be responsible for the origin of type-II superconductivity. However, it requires further theoretical analysis to understand the underlying superconductivity in  $\beta$ -W films.

## References

- <sup>1</sup> Gibson, J.W. and Hein, R.A., Superconductivity of tungsten. *Phys. Rev. Lett.* **12**(25), 688 (1964).
- <sup>2</sup> Sengupta, S, Li C, Baumier, C, Kasumov, A, Guéron, S, Bouchiat, H, Fortuna, F. Superconducting nanowires by electron-beam-induced deposition. *Appl. Phys. Lett.* **106**, 042601(2015).
- <sup>3</sup> Kondo, S. Superconducting characteristics and the thermal stability of tungsten-based amorphous thin films. *J. Mater. Res.* **7**, 853-60 (1992).
- <sup>4</sup> Sun, Y, Wang, J, Zhao, W, Tian, M, Singh, M, Chan, MH. Voltage-current properties of superconducting amorphous tungsten nanostrips. *Sci. Rep.* **3**, 2307 (2013).
- <sup>5</sup> Charlton, M. G., Davis, G. L. Allotropes of tungsten. *Nature.* **175**, 131-2 (1955).
- <sup>6</sup> Basavaiah, S, Pollack, S. R. Superconductivity in  $\beta$ -Tungsten Films. *J. Appl. Phys.* **39**, 5548-56 (1968).
- <sup>7</sup> Xu, X. A review and prospects for Nb<sub>3</sub>Sn superconductor development. *Supercond. Sci. Technol.* **30**, 093001 (2017).
- <sup>8</sup> Devantay, H., Jorda, J. L., Decroux, M., Muller, J., Flükiger, R. The physical and structural properties of superconducting A15-type Nb-Sn alloys. *J. Mater. Sci.* **16**, 2145-53 (1981).
- <sup>9</sup> Vink, T. J., W. Walrave, J. L. C. Daams, A. G. Dirks, M. A. J. Somers, and K. J. A. Van den Aker. "Stress, strain, and microstructure in thin tungsten films deposited by dc magnetron sputtering." *J. Appl. Phys.* **74**, 988-995 (1993).
- <sup>10</sup> O'keefe, M. J., and J. T. Grant. "Phase transformation of sputter deposited tungsten thin films with A-15 structure." *J. Appl. Phys.* **79**, 9134-9141(1996).
- <sup>11</sup> Shen, Y.G. and Mai, Y.W., Influences of oxygen on the formation and stability of A15  $\beta$ -W thin films. *Mater. Sci. Eng. A.* **284**, 176-83 (2000).
- <sup>12</sup> Lee, J.S., Cho, J. and You, C.Y., Growth and characterization of  $\alpha$  and  $\beta$ -phase tungsten films on various substrates. *J. Vac. Sci. Technol. A.* **34**, 021502 (2016).
- <sup>13</sup> Choi, D., Wang, B., Chung, S., Liu, X., Darbal, A., Wise, A., Nuhfer, N.T., Barmak, K., Warren, A.P., Coffey, K.R. and Toney, M.F., Phase, grain structure, stress, and resistivity of

sputter-deposited tungsten films. *J. Vac. Sci. Technol. A: Vacuum, Surfaces, and Films* **29**, 051512 (2011).

<sup>14</sup> Testardi, L. R. Destruction of superconductivity by laser light. *Phys. Rev. B.* **4**, 2189 (1971).

<sup>15</sup> Kammerer, O. F. and Strongin, M. Superconductivity in tungsten films. *Phys. Lett. A* **17**(3), 224 (1965).

<sup>16</sup> Chopra, K.L., Enhancement of superconductivity in tungsten films. *Phys. Lett. A* **25**(6), 451-452 (1967).

<sup>17</sup> Majkova, E., Luby, S., Jergel, M., Löhneysen, H.V., Strunk, C. and George, B. Superconductivity and critical fields in amorphous tungsten/silicon multilayers. *Physica Status Solidi (a)*, **145**(2), 509-519 (1994).

<sup>18</sup> Surick, J. J., Growth of amorphous tungsten silicide and study of the proximity effect at low dimensions for superconducting applications (Doctoral dissertation, Massachusetts Institute of Technology, 2015).

<sup>19</sup> Zhang, X., Lita, A.E., Sidorova, M., Verma, V.B., Wang, Q., Nam, S.W., Semenov, A. and Schilling, A. Superconducting fluctuations and characteristic time scales in amorphous WSi. *Phys. Rev. B* **97**(17), 174502 (2018).

<sup>20</sup> Hägg, G., Schönberg, N.,  $\beta$ -Tungsten as a tungsten oxide. *Acta Crystal.* **7**, 351-2 (1954).

<sup>21</sup> Morcom, W. R., W. L. Worrell, H. G. Sell, and H. I. Kaplan. "The preparation and characterization of beta-tungsten, a metastable tungsten phase." *Metallurgical transactions* **5**, 155 (1974).

<sup>22</sup> Chattaraj, A., Balal, M., Yadav, A.K., Barman, S.R., Sinha, A.K., Jha, S.N., Joulie, S., Serin, V., Claverie, A., Kumar, V. and Kanjilal, A., Unravelling oxygen driven  $\alpha$  to  $\beta$  phase transformation in tungsten. *Sci. Rep.* **10**, 14718 (2020).

<sup>23</sup> Chattaraj, A., Joulie, S., Serin, V., Claverie, A., Kumar, V. and Kanjilal, A., Crucial role of oxygen on the bulk and surface electronic properties of stable  $\beta$  phase of tungsten. *Sci. Rep.* **12**, 3865 (2022).

<sup>24</sup> Lita, A.E., Rosenberg, D., Nam, S., Miller, A.J., Balzar, D., Kaatz, L.M. and Schwall, R.E., Tuning of tungsten thin film superconducting transition temperature for fabrication of photon number resolving detectors. *IEEE Trans. Appl. Supercond.* **2005**, 15, 3528-31.

- <sup>25</sup> Irwin, K.D., Cabrera, B., Tigner, B. and Sethuraman, S. Tungsten thin films for use in cryogenic particle detectors. In Low temperature detectors for neutrinos and dark matter Pt. 4 1992.
- <sup>26</sup> Ozaki, K., Hanatani, T. and Nakamura, T., Analysis of crystalline phases in airborne particulates by grazing incidence X-ray diffractometry. *Analyst* **130**, 1059-64 (2005).
- <sup>27</sup> Chattaraj, A., Khan, S., Walczak, L. and Kanjilal, A., Probing the impact of surface reactivity on charge transport in dimensional phase changed tungsten films. *J. Mater. Sci.: Mater. Electron* **30**, 8278-85 (2019).
- <sup>28</sup> Purushotham, E. and Krishna, N.G., X-ray determination of crystallite size and effect of lattice strain on Debye–Waller factors of platinum nano powders. *Bul. Mater. Sci.* **36**, 973-6 (2013).
- <sup>29</sup> Ooi, Z.V., Saif, A.E.A., Wahab, Y. and Jamal, Z.A.Z., X-ray line profile analysis of BaTiO<sub>3</sub> thin film prepared by sol-gel deposition. *AIP Conf. Proc.* **1835**(1), 020011 (2017).
- <sup>30</sup> Petroff, P., Sheng, T.T., Sinha, A.K., Rozgonyi, G.A. and Alexander, F.B., Microstructure, growth, resistivity, and stresses in thin tungsten films deposited by rf sputtering. *J. Appl. Phys.* **44**, 2545-54 (1973).
- <sup>31</sup> Girault, B., Eyidi, D., Goudeau, P., Sauvage, T., Guérin, P., Bourhis, E.L. and Renault, P.O., Controlled nanostructuring of polycrystalline tungsten thin films. *J. Appl. Phys.* **113**, 174310 (2013).
- <sup>32</sup> Chen, C., Das, P., Aytan, E., Zhou, W., Horowitz, J., Satpati, B., Balandin, A.A., Lake, R.K. and Wei, P., Strain-Controlled Superconductivity in Few-Layer NbSe<sub>2</sub>. *ACS Appl. Mater. Interfaces* **12**, 38744-50 (2020).
- <sup>33</sup> Pogrebnyakov, A.V., Redwing, J.M., Raghavan, S., Vaithyanathan, V., Schlom, D.G., Xu, S.Y., Li, Q., Tenne, D.A., Soukiassian, A., Xi, X.X. and Johannes, M.D., Enhancement of the Superconducting Transition Temperature of MgB<sub>2</sub> by a Strain-Induced Bond-Stretching Mode Softening. *Phys. Rev. Lett.* **93**, 147006 (2004).
- <sup>34</sup> Chandra, L.S., Chattopadhyay, M.K., Chandra, J., Manekar, M.A., Pandey, S.K., Venkatesh, R. and Roy, S.B., Internal strain induced superconductivity in arc melted Ti<sub>0.97</sub>Fe<sub>0.03</sub> alloy. *Supercond. Sci. Technol.* **31**, 085004 (2018).

- <sup>35</sup> Ahadi, K., Galletti, L., Li, Y., Salmani-Rezaie, S., Wu, W. and Stemmer, S., Enhancing superconductivity in SrTiO<sub>3</sub> films with strain. *Sci. Adv.* **5**(4), eaaw0120 (2019).
- <sup>36</sup> Herrera, C., Cerbin, J., Jayakody, A., Dunnett, K., Balatsky, A.V. and Sochnikov, I., Strain-engineered interaction of quantum polar and superconducting phases. *Phys. Rev. Mater.* **3**, 124801 (2019).
- <sup>37</sup> Ma, F., Zheng, H.B., Sun, Y.J., Yang, D., Xu, K.W. and Chu, P.K., Strain effect on lattice vibration, heat capacity, and thermal conductivity of graphene. *Appl. Phys. Lett.* **101**, 111904 (2012).
- <sup>38</sup> Wu, X., Cai, Y., Bian, J., Su, G., Luo, C., Yang, Y. and Zhang, G., Strain engineering and lattice vibration manipulation of atomically thin TaS<sub>2</sub> films. *RSC Adv.* **10**, 16718-26 (2020).
- <sup>39</sup> Choi, J., Kim, Y.K., Kim, C.D., Kim, S. and Jo, Y., Enhancing the critical temperature of strained Niobium films. *Mater. Res. Exp.* **7**, 076001 (2020).
- <sup>40</sup> Mata-Pinzón, Z., Valladares, A.A., Valladares, R.M. and Valladares, A., Superconductivity in bismuth. A new look at an old problem. *PLoS ONE*, **11**(1), p.e0147645 (2016).
- <sup>41</sup> Gastiasoro, M.N. and Andersen, B.M., Enhancing superconductivity by disorder. *Phys. Rev. B.* **98**, 184510 (2018).
- <sup>42</sup> Dodaro, J.F. and Kivelson, S.A., Generalization of Anderson's theorem for disordered superconductors. *Phys. Rev. B.* **98**, 174503 (2018).
- <sup>43</sup> Deutscher, G., The Role of the Short Coherence Length in Unconventional Superconductors. *Condens. Matter* **5**, 77 (2020).
- <sup>44</sup> Moshe, A.G., Farber, E. and Deutscher, G., From orbital to Pauli-limited critical fields in granular aluminum films. *Phys. Rev. Research* **2**, 043354 (2020).
- <sup>45</sup> Tinkham, M., Effect of fluxoid quantization on transitions of superconducting films. *Phys. Rev.* **129**, 2413 (1963).